nature communications

Article

https://doi.org/10.1038/s41467-026-77988-x

Approaching Landauer's limit in a single superconducting vortex memory bit

Received: 4 December 2025

Accepted: 8 September 2026

Published online: 24 September 2026

Check for updates

Nofar Fridman[1,2] ✉, Itai Keren[1,2], Avia Noah[3], Yishay Zur[1,2], Martin E. Huber[4], Nadav Katz[1,2,5], Roland Willa[6,7,8], Hadar Steinberg[1,2] ✉ & Yonathan Anahory[1,2] ✉

This work investigates the energy required to manipulate a memory bit using a superconducting vortex confined in a nanoscale double-well pinning potential. In the experiments, various double-well systems subjected to sinusoidal forces is explored, and the effects of both driving force and frequency is analyzed. Results reveal characteristic stochastic resonance behavior for weak drives and adiabatic manipulation at strong, low-frequency drives. Although our experimental method requires a steady sinusoidal drive incompatible with Landauer's erasure protocol, our numerical analysis demonstrates that the work required for such bit manipulation (erasure) is within an order of magnitude of Landauer's limit ($k_BT\ln 2$) at 4.2 K. These findings open possibilities for creating highly efficient memory elements that could be integrated with cryogenic quantum circuits or function as topological quantum computing qubits; thereby contributing to memory devices with lower energy consumption and mitigating the escalating global energy demand in the computing industry.

Dissipation is crucial in nearly all areas of physical and applied sciences, with its significance further highlighted by Landauer's seminal work, which linked dissipation to information storage in a memory bit[1]. One such memory bit can be encoded in the position of a superconducting vortex[2], which is a candidate for a low-energy consumption classical memory compatible with the cryogenic environment of current quantum computers[3]. Furthermore, a detailed understanding of vortex dissipation impacts quantum technologies more broadly; for example, vortex dynamics contribute to decoherence in superconducting qubits[4,5] and fundamentally affect proposed vortex-based topological quantum information platforms[6–8].

The problem of many-body vortex matter phases has been extensively studied since the 1990s. Those works probed vortex dynamics involving micrometer displacements at high velocities (km/s) and high vortex concentrations[9–11]. Dissipation was measured by tracking the electric resistance and the out-of-phase components of the magnetic susceptibility[12]. Later, local probes have allowed to zoom in on the single-vortex response under periodic excitation in the low-amplitude limit[13–19]. In some of these studies, local dissipation was detected for AC vortex nucleation[19] and thermal activation near T_c[13,14]. Although these works clearly show the presence of dissipation, none of them provides a quantitative estimate.

The low dissipation of single-vortex motion renders its evaluation a formidable experimental challenge. Foltyn et al.[20] expel a single vortex from the superconductor over a length of 200 − 300 nm and show that the resulting dissipation, which gives rise to a local temperature increase of ∼ 0.25 K, is evaluated to ∼ 4×10^{-19} J per

[1]The Racah Institute of Physics, The Hebrew University, Jerusalem, Israel. [2]Center for Nanoscience and Nanotechnology, Hebrew University of Jerusalem, Jerusalem, Israel. [3]Faculty of Engineering, Ruppin Academic Center, Monash, Israel. [4]Departments of Physics and Electrical Engineering, University of Colorado Denver, Denver, CO, USA. [5]Qarakal Quantum Ltd., Tel Aviv, Israel. [6]Institute of Systems Engineering, School of Engineering, HES-SO Valais-Wallis, rue de l'Industrie, Sion, Switzerland. [7]Institute for Theory of Condensed Matter, Karlsruhe Institute of Technology, Karlsruhe, Germany. [8]Heidelberger Akademie der Wissenschaften, Heidelberg, Germany. ✉e-mail: nofarfri.friedman@mail.huji.ac.il; hadar.steinberg@mail.huji.ac.il; yonathan.anahory@mail.huji.ac.il

operation at 400 mK. Similar dissipation ($\sim 10^{-18}$ J) was estimated for the creation of a Josephson vortex at 4 K [21].

An essential tool for detecting single-vortex motion is the SQUID-on-tip (SOT) microscope, which exhibits high magnetic sensitivity and fine spatial resolution[17,22–24]. SOT probes have also proven to be extremely sensitive local thermometers, achieving a sensitivity of 4×10^{-14} W at 4 K[25]. This sensitivity, however, is barely sufficient for detecting the power dissipated by a single vortex driven periodically at our maximum bandwidth (150 kHz), even if the heat released for each period is 4×10^{-19} J. It is, hence, unrealistic to detect the dissipation of vortices moving on the nanometer scale using SOT thermometry. Moreover, inferring the heat dissipated by measuring the temperature change requires detailed modeling of the heat flow, including tip-sample and electron-phonon coupling, as well as the Kapitza resistance between different materials.

This work builds on previous studies[13,14,17], to provide a quantitative measure of the dissipation of individual vortices under periodic drive. By measuring the magnetic signal modulation induced by vortex motion, the average work per cycle can be directly assessed without relying on temperature measurements, thereby circumventing the difficulties associated with modeling heat flow. Applying this method, we measure dissipation orders of magnitude below those achieved in previous works, reaching levels below Landauer's limit[1] of $k_BT\ln(2)$.

Results

A Nb film of thickness $d = 55$ nm was grown and patterned into a 10 μm-wide bridge (Fig. 1a, see Methods). The value of d was chosen to be on

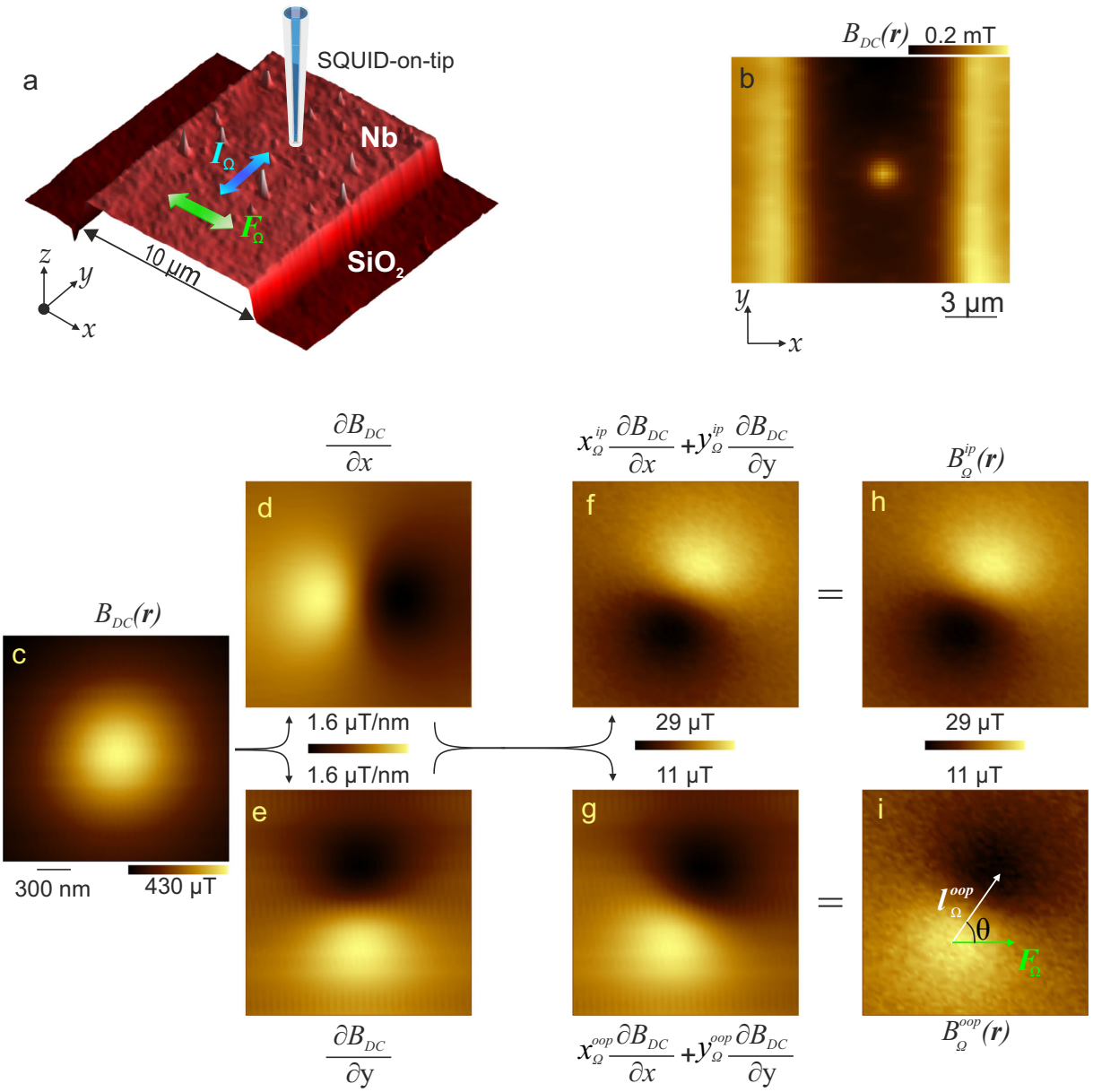


Fig. 1 | Experimental setup. a 3D representation of a 16 × 13 μm² AFM image of the 55 nm-thick Nb film patterned into a 10 μm-wide strip. Indicated are the direction of the applied oscillating current I_Ω (blue double-headed arrow) and the resulting Lorentz force F_Ω acting on the vortices at the driving frequency Ω (green double-headed arrow). **b**, **e** SQUID-on-tip images of the z component of the magnetic field. **b** DC magnetic image of the out of plane field $B_{DC}(r)$ of a single vortex pinned on the Nb strip. **c** A zoomed-in image of the measured $B_{DC}(r)$ of a vortex. **d**, **e** Numerical derivatives $\frac{\partial B_{DC}}{\partial x}$ **d** and $\frac{\partial B_{DC}}{\partial y}$ **e**, of the image shown in (**c**). **f** $x_\Omega^{ip}\frac{\partial B_{DC}}{\partial x}+y_\Omega^{ip}\frac{\partial B_{DC}}{\partial y}$ with $x_\Omega^{ip}=-7.4$ nm and $y_\Omega^{ip}=-15.4$ nm values obtained by fit to **h** (**g**) Same as **f** but for the out-of-phase (oop) component with $x_\Omega^{oop}=3.2$ nm and $y_\Omega^{oop}=6.5$ nm values obtained by fit to (**i**). **h**–**i** Experimentally measured $B_\Omega^{ip}(r)$ **h** and $B_\Omega^{oop}(r)$ **i** of the vortex driven by $F_\Omega=93$ fN at 19 kHz acquired simultaneously with c.

the same order as the coherence length $\xi = 12$ nm and the London penetration depth $\lambda = 220$ nm. In this case, the vortex can be regarded as a particle in a random 2D potential landscape (Supplementary Note 1). The sample was then mounted in a scanning SOT microscope to image the out-of-plane component of the magnetic field at 4.2 K (see "Methods" and refs. 21,22). A protocol was established to obtain a single vortex within an area of at least 5×5 μm^2 as shown in Fig. 1b (see "Methods"). The vortex was subject to a periodic force by applying a current, $I_\Omega = I_0 \cos(\Omega t)$, along the bridge (blue double-headed arrow in Fig. 1a). The resulting Lorentz force is given by $\boldsymbol{F}_\Omega(x,t) = \Phi_0 J_\Omega(x)\hat{x} = F_\Omega \cos(\Omega t)\hat{x}$, where Φ_0 is the magnetic flux quantum and $J_\Omega(x) = \frac{I_\Omega}{\pi\sqrt{(w_b/2)^2 - (x)^2}}$ is the sheet current density at a distance x from the center of the bridge of width w_b as calculated in ref. 26. For example, for a typical current of $I = 0.5$ mA, we obtain $J(0) \approx 31.8$ A/m, and $F_\Omega = 65$ fN $\hat{x}$ (green double-headed arrow in Fig. 1a). The relevant force scale was determined experimentally from the observed crossover between linear and nonlinear response as discussed below. The vortex-tip interaction was measured to ~ 7 fN at our scanning distance of 300 nm (Supplementary Note 2), which is comparable to the smallest driving forces F_Ω and can be partially compensated by a constant current I_{DC}.

The periodic force displaces the vortex away from its equilibrium position, resulting in a time-dependent magnetic field, $B(\boldsymbol{r}, t)$. Our methodology relies on measuring the Fourier components of $B(\boldsymbol{r}, t)$ with a lock-in amplifier. In general, $B(\boldsymbol{r}, t)$ can be expressed as $B_\Omega(\boldsymbol{r}, t) = \sum_{n=1}^{\infty} B^{ip}_{n\Omega}(\boldsymbol{r}) \cos(n\Omega t) + B^{oop}_{n\Omega}(\boldsymbol{r}) \sin(n\Omega t)$, where $B^{ip}_{n\Omega}(\boldsymbol{r})$ and $B^{oop}_{n\Omega}(\boldsymbol{r})$ represent the magnetic field amplitude modulation of the n-th harmonic that is in-phase (ip) and out-of-phase (oop) with respect to the phase of the driving current I_Ω, and $\boldsymbol{r}$ is the coordinate of the SOT. The reference phase is set so that the magnetic field caused by the current, according to the Biot-Savart law, is detected solely in the ip signal (see Supplementary Note 3 and Supplementary Fig. 1). The scanning SOT microscope simultaneously measures the spatial distributions of the DC magnetic field $B_{DC}(\boldsymbol{r})$ (Fig. 1c) and of the 1st harmonic AC field $B^{ip}_\Omega(\boldsymbol{r})$ and $B^{oop}_\Omega(\boldsymbol{r})$ (Fig. 1h, i). For small displacements of the vortex, the AC and DC field images are related by $B^{ip}_\Omega(\boldsymbol{r}) = x^{ip}_\Omega \frac{\partial B_{DC}}{\partial x} + y^{ip}_\Omega \frac{\partial B_{DC}}{\partial y}$, where x^{ip}_Ω and y^{ip}_Ω are displacement amplitudes at frequency Ω, in-phase with the applied force, along the x and y axis, respectively. Using this relation, we measure the ip and oop displacement amplitudes independently as illustrated in Fig. 1c–i. The very high sensitivity of the SOT allows us to measure sub-nm displacements[17]. The displacement sensitivity is roughly estimated by dividing the SOT and RMS electronic noise background in a typical $\Delta S_{B_\Omega} \sim 250$ nT by the maximum vortex DC field gradient $\max \frac{\partial B_{DC}}{\partial x} = 0.8$ μT/nm, which give a displacement sensitivity of $\Delta S_{x_\Omega} \sim 0.3$ nm.

For the rest of this article, we will use polar coordinates $l^{ip}_\Omega = \sqrt{\left(x^{ip}_\Omega\right)^2 + \left(y^{ip}_\Omega\right)^2}$, and θ is the angle with respect to the Lorentz force as depicted in Fig. 1i. The angle between the applied force and the vortex motion arises from the anisotropy of the pinning potential and has been discussed in prior works[17,18].

We calculate the work exerted by the Lorentz force on the vortex $W = \oint \vec{F} \cdot d\vec{l} = \cos(\theta) \int_0^{2\pi/\Omega} F_\Omega \cos(\Omega t) \frac{dl}{dt} dt$, where the vortex position is expressed in terms of its Fourier components:

$l(t) = \sum_{n=1}^{\infty} l^{ip}_{n\Omega} \cos(n\Omega t) + l^{oop}_{n\Omega} \sin(n\Omega t)$. Substituting $\frac{dl}{dt}$ into the integral, all the terms of the Fourier series vanish except the term in l^{oop}_Ω, which results in $W = \pi \cos(\theta) F_\Omega l^{oop}_\Omega$. Given that the average temperature is constant in time, the work exerted on the vortex is equal to the energy dissipated by the vortex.

The dissipation associated with motion in a single-well harmonic potential, as depicted in our toy model Fig. 2a, c, is estimated to $W \sim 10^{-25}$ J per cycle (Supplementary Note 4), which is too low to detect experimentally. Thus, we observe $B^{ip}_\Omega \neq 0$ and $B^{oop}_\Omega = 0$, which is expected for the motion of an overdamped particle where the applied force is always equal to the restoring force. However, a double-well potential, as depicted in Fig. 2b, d, provides an interesting experimental platform. With our SOT, we resolve—and subsequently study—such a double-well pinning landscape. We search for double-well potentials by exploring distinct equilibrium positions on the sample. By sweeping I_{DC} we tilt the potential landscape, moving the average position of the vortex across the sample. For certain values of I_{DC}, in addition to the oscillating current I_Ω, a sharp increase of B^{oop}_Ω is detected. It systematically coincides with the appearance of higher harmonics in $B(\boldsymbol{r}, t)$. This rise in the measured work is interpreted as periodic vortex jumps over an energy barrier that separates two local potential minima (Fig. 2b, d). The telegraphic noise measured exclusively when positioning the SOT loop near an undriven vortex confirms this hypothesis (Supplementary Fig. 2).

Figure 3 shows the work W and displacement $l_\Omega = \sqrt{(l^{ip}_\Omega)^2 + (l^{oop}_\Omega)^2}$ for three sets of double-well systems as a function of the driving force amplitude F_Ω in the presence of a fixed I_{DC} for two driving frequencies Ω. We first discuss the common features for l_Ω seen in all double-well systems presented here. Below a critical driving force $F_\Omega < F_c$, the displacement l_Ω is homogeneous ($F_\Omega = k l_\Omega$), demonstrating that the vortex oscillation occurs in an overdamped harmonic potential with a spring-constant k (Supplementary Fig. 3). As

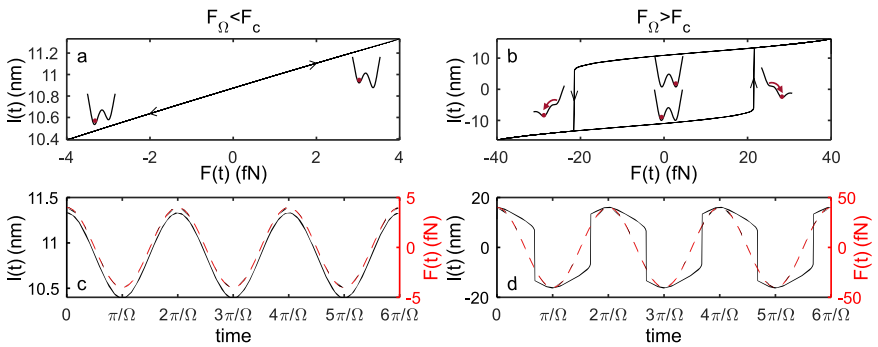


Fig. 2 | One-dimensional toy model of an overdamped double-well potential. **a** Position $l(t)$ vs. applied force $F(t)$ for a vortex oscillating at low amplitude within the left well as depicted in the insets. **b** Same as **a**, for larger driving force amplitude F_Ω. The area between the curves corresponds to the vortex dissipation throughout one cycle. **c** Time trace of the solution $l(t)$ in (**a**). The solution follows the sinusoidal trend of the external force. **d** Time trace of the solution given in (**b**). Here we observe the apparition of phase delay and higher harmonics. The purpose of this figure is to illustrate the expected physics. None of the curves shown in this figure correspond to measured experimental data or to the Monte Carlo simulations used for quantitative comparison.

https://doi.org/10.1038/s41467-026-77988-x

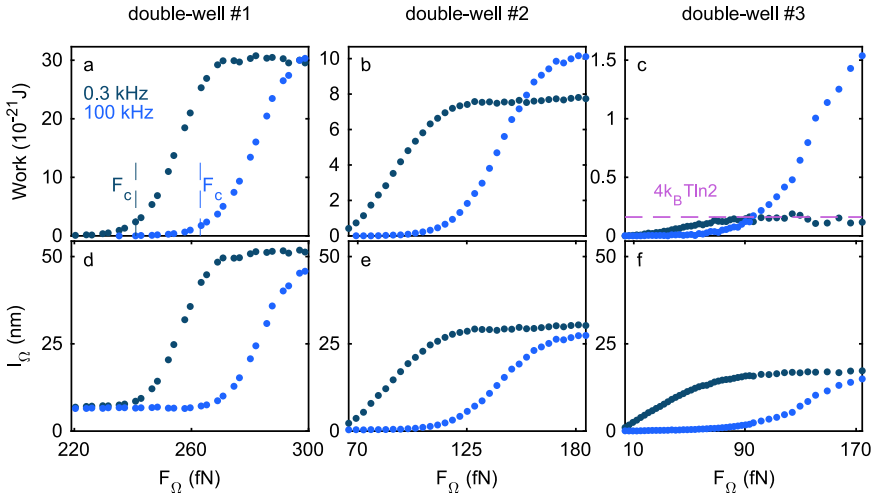


Fig. 3 | Work and displacement as a function of the driving force. (**a**-**c**) Average work per period W as a function of the driving force F_Ω for three double-well potentials located at distinct sample positions. Two driving frequencies $\Omega = 0.3$, 100 kHz are plotted in dark and light blue, respectively. (**a**) Vertical dashed curves indicate the critical force F_c at which $W > 0$. (**c**) The pink dashed line marks four times Landauer's limit. (**d**-**f**) Vortex displacement amplitude $l_\Omega = \sqrt{(l_\Omega^{ip})^2 + (l_\Omega^{oop})^2}$, as a function of the driving force F_Ω.

the force reaches $F_\Omega \approx F_c$, $l_\Omega(F_\Omega)$ starts deviating from the harmonic behavior. Notably, for such strong drives, the total real-space displacement amplitude is not equal to l_Ω due to the presence of higher harmonics. However, our analysis only requires to measure l_Ω and W, which are measured properly even in presence of higher harmonics. Finally, at even higher driving forces $F_\Omega > F_c$, the harmonic behavior is recovered since the barrier can be neglected in the strong drive limit. The value of I_{DC} was chosen to minimize F_c and kept constant for a particular double-well. The general features found here are independent of small I_{DC} changes (see Supplementary Note 5).

We use $W = \pi \cos(\theta) F_\Omega l_\Omega^{oop}$ to extract the average work per cycle (Fig. 3a–c). In general, for all investigated double-well sets, for $F_\Omega < F_c$, no work is detected, which is consistent with a vortex trapped in one of the two minima. For stronger drives ($F_\Omega \approx F_c$), the vortex hops occasionally between the two adjacent wells. The vortex hopping to the bottom of the adjacent well, causes a delay in its return and hence a hysteretic force-displacement trajectory (Fig. 2b, d). The result is a sharp increase in the expected work. For $F_\Omega \gg F_c$, we find, once more, that the work remains constant, indicating that no significant additional work is performed as the vortex systematically jumps over the barrier in each half-cycle. The work obtained for strong drives varies significantly between different double-well systems. Notably, the work per cycle can be as low as four times Landauer's limit (light purple dashed line in Fig. 3c). The origin of the factor four will be discussed below. This has immense potential for low-energy consumption memory devices.

We now turn to the effect of the driving frequency Ω. For the displacement l_Ω, in all three double-well systems reported in Fig. 3, an increasing frequency causes an increase in F_c. In all these cases, the asymptotic values of l_Ω at both weak and strong driving forces remain approximately unchanged. The change in F_c can be explained by thermal activation, which plays a greater role at low frequencies. Turning to the dependence of the work W on Ω, we find the same change in F_c: For well #1, the work for $F_\Omega > F_c$ remains unchanged within our uncertainty. However, for well #2, we detect a 25% change in the measured work for large F_Ω. That relative difference is much larger for well #3, where work increases by a factor of ~ 10 compared to the low driving frequency. We argue here that the evolution of the work with driving force and frequency is a consequence of vortex dynamics in the double-well system at finite temperature. The distinct properties of those double-well systems can be unified within a single model, where the dynamics are explained in terms of the height of the energy barrier E_b between the two wells and the distance between the two minima $2l_0$.

Our model is based on a one-dimensional Monte-Carlo simulation, assuming a double-well potential, as described in detail in the Methods section. A sinusoidal driving force, matching the Lorentz force applied in experiment, tilts the pinning potential. For each time interval dt, the total potential $U_{tot} = U_{pin} + F_\Omega(t) l(t)$ is calculated. The vortex position $l(t)$ always corresponds to a local minimum point of U_{tot} at that time, which means that we ignore the inertia term (overdamped regime). We assume that the typical hopping rate is Kramer's rate $r_K = r_0 e^{-E_b/kT}$, where r_0 is the trial frequency. If the vortex jumps over the barrier, we consider instantaneous vortex energy relaxation to align with the potential energy at the new location, implying energy dissipation. We assume that a constant temperature steady state is reached, so the dissipation of energy from the vortex to the bath is equal in magnitude to the work exerted upon it. The average work and displacement per cycle are calculated to be compared with the measured work.

To test the validity of the model, in Fig. 4, we map W and l_Ω as a function of Ω, given distinct driving force amplitude F_Ω for the same double-well sets #1 and #2, presented above in Fig. 3. For double-well #1, which is the most dissipative and has the largest F_c, the vortex displacement l_Ω is frequency independent in both weak (blue curve) and strong (red curve) drive limits (Fig. 3a). Intuitively, for weak drives, the vortex is trapped in one of the two harmonic potential wells where no frequency dependence is expected (see Supplementary Fig. 4 and Note 5). For strong drives, the vortex hops systematically between the two wells, and the energy barrier E_b can be neglected, resulting in a broader harmonic potential with frequency-independent work (Fig. 4c). The intermediate regime, where l_Ω and W scale as $1/\Omega$ over most of the frequency range, is where stochastic effects become significant. Notably, our simulations capture all the features discussed above except for the experimental noise, which becomes visible in the low-dissipation regime ($W \lesssim 10^{-23}$ W). This noise originates from the finite field sensitivity of the SOT and its readout electronics. Double-well #2 exhibits the same features, although it was not probed well into the to the weak drive limit. This regime will be discussed in the following section.

Stochastic resonance theory provides a valuable framework for discussing thermal activation between wells[27]. Taking the limit of perturbative drives, where the external force does not alter

https://doi.org/10.1038/s41467-026-77988-x

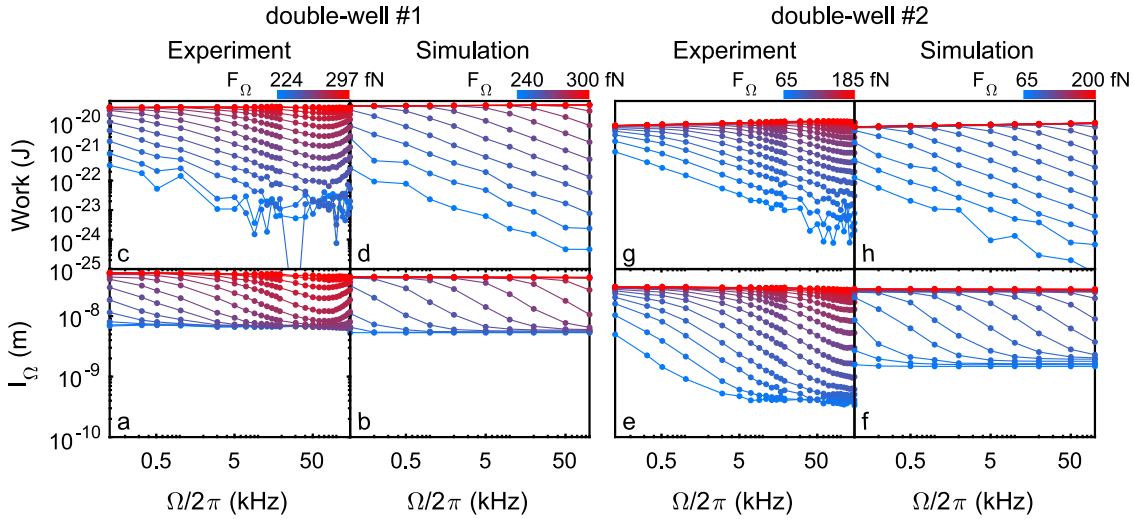


Fig. 4 | Measured and simulated displacement and work as functions of the driving frequency. a, **b**, **e**, **f** Displacement $l_\Omega = \sqrt{(l_\Omega^{ip})^2 + (l_\Omega^{oop})^2}$, as a function of the driving frequency Ω for double-well # 1 **a**, **b**, and double-well #2, **e**, **f**. Experimental data are shown in (**a**, **e**); simulations in (**b**, **f**). **c**, **d**, **g**, **h** Same as **a**, **b** and **e**, **f**, but showing the work W as a function of Ω. Experimental data are shown in **c**, **g**; simulations in (**d**, **h**). Each curve depicts the measured l_Ω or W for a given driving force F_Ω. The color of each curve represents F_Ω as indicated by the respective color bars.

significantly E_b, the average displacement is described analytically as:

$$l_\Omega = \frac{2F_\Omega l_0 r_k}{k_B T\sqrt{4r_k^2+\Omega^2}} \quad (1)$$

The same framework is used to evaluate the work, which is expected to peak when $\Omega \approx r_k$

$$W = \frac{2\pi F_\Omega^2 l_0^2 r_k \Omega}{k_B T\left(4r_k^2+\Omega^2\right)} \quad (2)$$

Our numerical simulations demonstrate that r_k of the undriven vortex ($F_\Omega = 0$) is far too small to be measured: $r_k = 10^{-45}$ and 10^{-6} Hz for double-wells #1 and #2, respectively. In contrast, double-wells #3 and #4 present an opportunity to study a system where thermally activated jumps occur in the perturbative drive limit while placing r_k within our experimental bandwidth. As shown in Fig. 5, we measure displacement and work starting with driving forces as low as $F_\Omega = 4$ fN and up to the strong drive limit where $F_\Omega > 100$ fN. At each driving force, we have access to 2 frequency regimes: $\Omega \ll r_k$, and $\Omega \gg r_k$. Figure 5 reports measurements on two sets of double-well potentials and their related simulations (double-wells #3 and 4). We find that stochastic physics is evidently in quantitative agreement with the analytic expressions in Eqs. 1 and 2, using only two fitting parameters for all the curves shown in magenta, for a given double-well. We note that for double-well #3, different values of $l_0 = 2.0$ and 3.9 ± 0.1 nm were used to fit W and l_Ω, respectively (see all l_0, listed in Supplementary Table 2). This small discrepancy is statistically significant but its origin remains unknown, although the fact that it was not observed in six other examples shown in Supplementary Fig. 5 suggests that it might be due to a small systematic error. In the strong drive limit where Eqs. 1 and 2 no longer apply, we can still rely on our numerical simulations, which agree well with the data. We can thus conclude that the stochastic resonance model provides a valid description of the dynamics of double-wells #3 and #4.

The average hopping frequency r_k can be independently probed for an undriven vortex. In this measurement, the SOT is held stationary and positioned at one of the lobes of the AC magnetic field image $B_\Omega(\boldsymbol{r})$, where the signal arising from vortex motion is maximal. In this configuration, the measured signal contains an additional telegraphic noise component originating from the stochastic vortex dynamics, as illustrated in the time domain for another double-well potential in Supplementary Fig. 2. We analyze this signal in the frequency domain by measuring the noise spectrum $B(\omega)$ at that location (Supplementary Fig. 6). The measured spectrum consists of two contributions: (i) the intrinsic background noise of the SOT, characterized independently when the tip is positioned far from the vortex, and (ii) a Lorentzian component associated with telegraphic noise, expected for a two-state stochastic process, with spectral dependence proportional to $1/\left(4r_k^2+\omega^2\right)$[27]. This contribution reflects the thermally activated transitions of the vortex between the two minima of the double-well potential. By fitting the measured spectra with this expression, we extract hopping rates of $r_k = 7 \pm 2$ kHz and $r_k = 3 \pm 1$ kHz for double wells #3 and #4, respectively. These values are consistent with those obtained independently from fitting the frequency dependence of the work $W(\Omega)$ and the first harmonic displacement $l_\Omega(\Omega)$ using Eqs. (1) and (2) in the weak-drive limit. This agreement provides further evidence for the stochastic nature of the vortex dynamics and strengthens the experimental basis for both the Monte Carlo simulations and the stochastic resonance analysis.

Discussion

Landauer's limit was approached or reached in systems where micrometer-scale colloidal particles are manipulated by optical tweezers over a length scale of 1 micron[28], in relatively large SQUID structures[29], and in single-molecule magnets[30]. An interesting outcome of Fig. 5 is that the work exerted on a vortex can assume values below Landauer's limit. This limit is of fundamental importance in computer science and sets a bound of $k_B T\ln(2)$ for the heat dissipated to irreversibly erase a memory bit[1]. In the following, we discuss how the parameters used to achieve such a low energy consumption manipulation cannot be used for a memory bit and therefore does not violate Landauer's limit. We demonstrate that using the double-wells presented here, the energy required to manipulate a memory bit indeed exceeds that fundamental limit but remains within the same order of magnitude.

The applicability of Landauer's limit in the different regimes of our experiment is outlined in Fig. 6a. For weak drives ($F_\Omega l_0 \ll E_b$), the vortex

https://doi.org/10.1038/s41467-026-77988-x

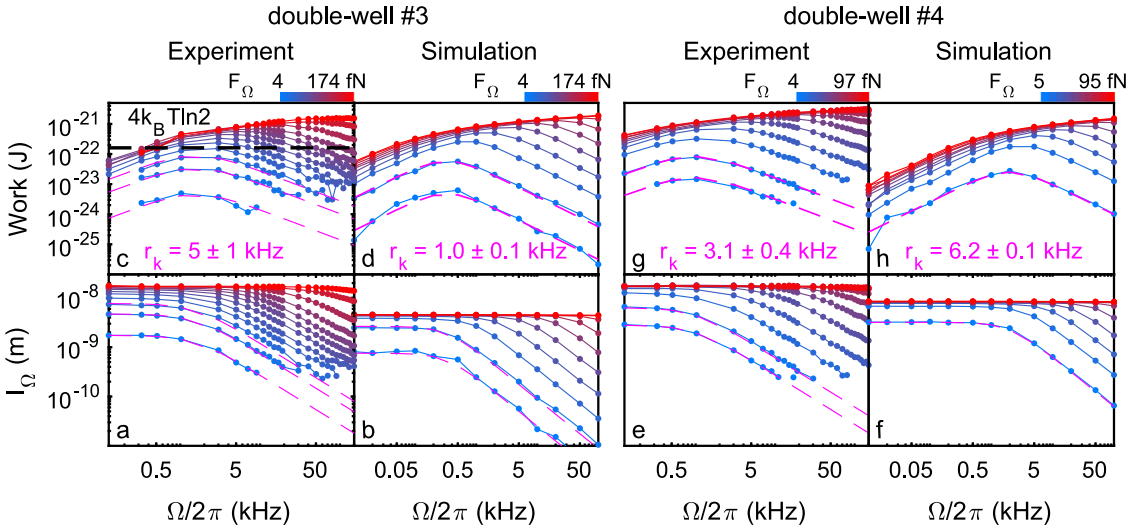


Fig. 5 | Measured and simulated vortex displacement and work for a small energy barrier. a, **b**, **e**, **f** Displacement $l_\Omega = \sqrt{(l_\Omega^{ip})^2 + (l_\Omega^{oop})^2}$, as a function of the driving frequency Ω for double-well # 3 **a**, **b** and double-well #4 **e**, **f**. Experimental data are shown in **a**, **e**; simulations in **b**, **f**. **c**, **d**, **g**, **h** Same as **a**, **b** and **e**, **f**, but showing the work W as a function of Ω. Experimental data are shown in **c**, **g**; simulations in (**d**, **h**). Each curve represents the measured l_Ω or W for a given driving force F_Ω. The color of each curve represents F_Ω as indicated by the respective color bars. The pink dashed curves correspond to Eqs. (1) and (2) using r_k values specified in the plot legend and l_0 values listed in Supplementary Table 2. The black dashed line marks four times Landauer's limit. Data points resulting from images that did not contain features above the noise level are not shown for clarity.

does not systematically hop over the barrier and therefore, Landauer's limit does not apply (Fig. 6a represented in blue). The strong drive limit ($F_\Omega l_0 \gg E_b$) is more nuanced: indeed, for such drives, the vortex is systematically shuttled between the two wells. However, this protocol is not initiated in a random state as assumed in Landauer's analysis. Our experimental method, based on Fourier analysis, imposes a continuous periodic drive and is thus incompatible with Landauer's erasure protocol. We emphasize that a true erasure protocol could in principle be implemented with the double-well potentials presented here, but our present measurement scheme would not allow direct measurement of the resulting dissipation.

This immediately raises the question of how to correctly compare the work measured with our experimental protocol with that required by the Landauer erasure protocol. We provide an answer by running our numerical simulation with a single-shot protocol: the simulation is initialized with an untilted potential, where the vortex is placed randomly in either of the two wells. The work on the vortex in the presence of a periodic force $F_\Omega(t) = F_\Omega \cos(\Omega t)$ is computed for a quarter period between $\Omega t_{\min} = \frac{3\pi}{2}$ (untilted) and $\Omega t_{\max} = 2\pi$ (fully tilted). This work calculation is repeated for 1000 cycles, and the average is taken.

We run this single-shot protocol using the same parameters employed above to simulate the potential landscapes of double-well #3 for the continuous protocol. Figure 6b compares the work resulting from the two protocols. For $\Omega \gg 2\pi r_k$, where stochasticity is not relevant, the work calculated for the single-shot protocol (black curve) is 4 times lower than the work simulated for the continuous protocol (blue curve, shown here with a factor 1/4). The factor 4 is comprised of a factor 2, related to the complete cycle, where two hopping events occur (back and forth), and another factor 2 related to the initial condition of the vortex. In Landauer's erasure protocol, the initial state of the memory is assumed to be random, with equal probability of being in state 0 or 1. If the system is coincidentally already in the target state, the erasure operation requires no work. As a result, on average, only half of the realization requires hopping over the barrier and thereby contributing to the erasure cost. In contrast, in our experimental protocol, the continuous sinusoidal drive effectively prepares the system in a well-defined initial state prior to each operation. As a result, the vortex must be driven across the barrier in every operation, leading to an average work that is larger by a factor of 2 compared to the Landauer protocol.

For $\Omega \ll 2\pi r_k$, the two situations differ. For the continuous protocol, the work is significantly lower than Landauer's limit, as observed in experiments and simulations. In contrast, the work calculated for the single-shot protocol remains above the limit, confirming the simulation's consistency with Landauer's principle. Notably, in such a regime, the vortex cannot serve as a memory bit since it cannot retain its information on that timescale. Therefore, in our case, a memory bit requires an energy penalty of ~5 times Landauer's limit at $\Omega/2\pi = 150$ kHz.

To further understand why continuous protocols allow work below Landauer's limit, we run the single-shot model for a half-cycle, allowing the system to return to the untilted potential. Figure 6b white curve highlights that this additional quarter cycle results in work well below Landauer's limit for $\Omega \ll 2\pi r_k$. This low work can be understood by considering that $\Delta S = k_B \ln 2$, which was added to the environment in the first quarter cycle (erasure), is returned to the vortex in the second quarter cycle (randomization), provided that the vortex has sufficient time to randomize ($\Omega \ll 2\pi r_k$). This process is analogous to adiabatic cooling (Fig. 6a represented in green).

Finally, our results allow us to evaluate the potential of vortices as low-dissipation memory elements. This could be achieved, for example, by integration with vortex control elements and readout as demonstrated in ref. 2. Practical memory devices require higher-frequency operation compared to the investigated range of Ω, limited by the bandwidth of our cryostat and SOT microscope. The question is whether higher frequency operation can be achieved without a significant penalty in the required work. In the case of double-wells #1 and #2, where Ω is at least eight orders of magnitude larger than r_k, we see that the work at large drive is frequency independent. It is reasonable to assume that for double-wells #3 and #4, the work per cycle will eventually saturate at a higher frequency. That trend is already visible within our experimental bandwidth. The operational frequency of such a vortex-based memory device would be limited by the shuttling time, which we estimate at 4 ns, corresponding to 250 MHz (Supplementary Note 6). These operational frequencies should be achieved with an energy cost $\approx 10 k_B T \ln 2$.

https://doi.org/10.1038/s41467-026-77988-x

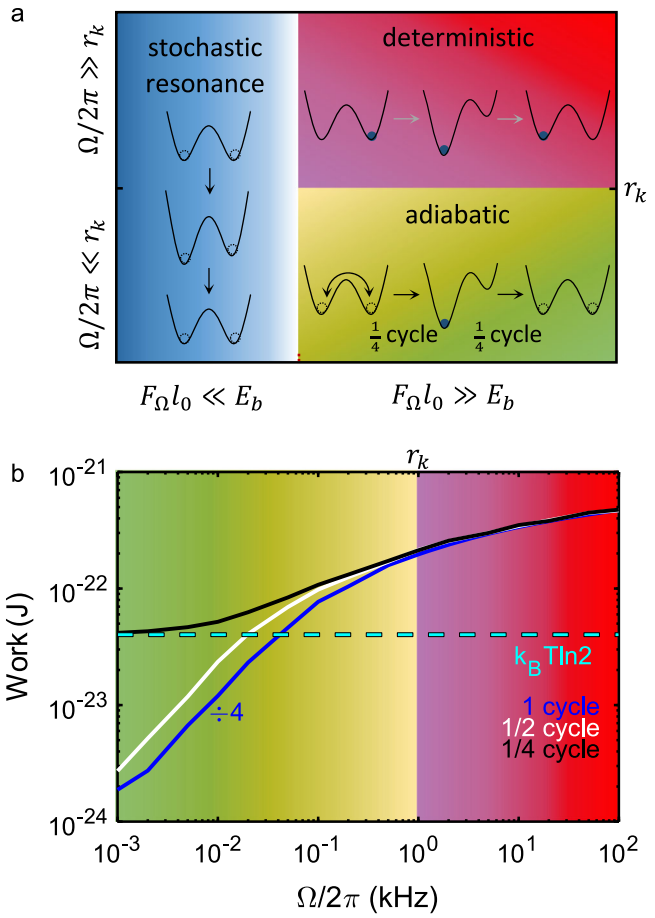


Fig. 6 | Work dissipation in distinct vortex memory protocols: comparison between Landauer's erasure (quarter-cycle), half-cycle, and full-cycle protocols. a Diagram of the distinct vortex-driving regimes. The region colored in blue is described by the stochastic resonance theory and is valid for perturbative drives F_Ω at all the driving frequencies Ω. The strong drive limit is divided into two regimes with respect to Ω. Far below Kramer's rate $\Omega \ll r_k = r_0 e^{-E_b/k_B T}$ corresponds to the adiabatic regime where the work per cycle vanishes (colored in green). For $\Omega \gg r_k$, the vortex hops systematically between the wells with no random jumps occurring (colored in red). Insets: schematic representation of the vortex total potential energy U_{tot} at distinct times during the cycle that differ by 1/4 cycle. Dark blue dots represent the deterministic vortex position, while the dashed line circle depicts the probabilistic vortex position with probability ≈ 1/2. **b** Simulation of the work as a function of Ω for three different vortex manipulation protocols under strong drive using the parameters that represent double-well # 3. (Black curve) Landauer's erasure protocol, starting from a random state in the untilted double-well potential and ending in the fully tilted potential, which corresponds to a quarter cycle. The plotted curve is the average of 1000 calculations. (White curve) Half-cycle protocol, identical to the Landauer's protocol with an additional quarter cycle, which ends with the potential being untilted as depicted in the inset of (**a**). (Blue curve) Full-cycle protocol corresponding to our measurement protocol as shown in Figs. 4 and 5. The background color code is the same as in **a**, red/green represent the deterministic/adiabatic regime.

Based on our results, one can envision using vortices as classical memory bits that interface with quantum computing elements. More exotic applications may involve the use of vortices in topological quantum computing protocols. Consequently, an essential prerequisite is adiabatic manipulation, in which vortices must be shuttled along sophisticated trajectories while retaining their ground state. The type of subgap vortex spectrum could be a determining factor here, which calls for future experiments with topological materials such as $FeTe_xSe_{1-x}$. The experimental methodology we provide here could be used to benchmark vortex manipulation operations and test their adiabaticity.

Methods

Sample fabrication

The Nb thin film was sputtered in a VST sputtering tool (TFDS-840), with a Kurt J. Lesker 2" Nb target (99.95% purity). The base pressure of the chamber was 3×10^{-7} Torr. Sputtering was carried out in a 5×10^{-3} Torr Argon for 60 s on a rotating 2" Si wafer at ambient (23 °C) temperature. The sample was then patterned by direct laser writing photolithography and reactive ion etching with Ar/SF_6.

SQUID-on-tip fabrication

The SOT was prepared using a self-aligned three-step process involving thermal deposition of Pb at cryogenic temperatures, as outlined in earlier works[22,23]. The SQUID loop employed in this work has a diameter of approximately 250 nm. This choice of a relatively larger diameter is strategic, as it provides magnetic sensitivity around the zero magnetic field found in the Meissner region of the sample. The larger diameter causes a lower period of the quantum interference pattern of the SQUID critical current versus applied field. This enhances the zero-field magnetic sensitivity, which is essential for measurements at low vortex densities. The tip-to-sample distance was set to 300 nm to be comparable with the tip diameter and to minimize the tip-vortex interactions (see Supplementary Note 2).

Single-vortex trapping protocol

To achieve a low-density vortex distribution, a current pulse exceeding the critical current I_c was applied along the bridge in the y-direction for a few seconds, under a near-zero out-of-plane magnetic field H_z. The resulting vortex distribution was mapped by imaging the static out-of-plane magnetic field $B_{DC}(\boldsymbol{r})$. This procedure was repeated, with fine magnetic field adjustments $\Delta H_z \lesssim 0.1$ mT, until a single isolated pinned vortex was obtained within an area of at least $5 \times 5\,\mu m^2$, as shown in Fig. 1b.

Numerical simulations

Our model is based on a one-dimensional numerical simulation where we assume a double-well potential that consists of two identical Lorentzians centered around $\pm x_0$, $U_{pin}(x) = \frac{-U_0}{1+(x+x_0)^2/(\xi_{eff})^2} + \frac{-U_0}{1+(x-x_0)^2/(\xi_{eff})^2}$[17,31], where ξ_{eff} is the well characteristic size and $U_0 \sim 10^{-20}$ J is the depth of each well. To obtain physical pinning sites, we consider $\xi_{eff} \gtrsim \xi = 12$ nm (Supplementary Fig. 7). The distance between the two wells, $2l_0 \sim 2x_0$, is set to match approximately the measured $2l_\Omega$ for strong drives. Here we distinguish between x_0, the simulation parameter for a given pin, and l_0, the distance between the two minima resulting from the sum of the two Lorentzians. A sinusoidal driving force, matching the force used at the respective double-well, tilts the pinning potential. For each time interval dt, the total potential $U_{tot} = U_{pin} + F_\Omega(t) l(t)$ is calculated. The vortex position $l(t)$ corresponds to a local minimum point of U_{tot} at that time. We assume that the typical hopping rate is Kramer's rate $r_K = r_0 e^{-E_b/k_B T}$, where r_0 is the trial frequency. To achieve this rate, a random number between 0 and 1 is picked. If the number is smaller than $r_K dt$, the vortex can overcome the barrier and move to the other local minimum; otherwise, the vortex remains in the same well. If the vortex jumps over the barrier, we assume instant vortex energy relaxation to match the potential energy at the new location. This way, if the vortex jumps from a high/low potential to a low/high potential, the work generated will be positive/negative. The work accumulated over the simulated time is divided by the number of cycles to be compared with the measured work. We assume that the vortex dissipation does not influence the bath temperature. The displacement l_Ω is calculated by applying a Fourier transform on the position of the vortex $l(t)$ and taking the component at

Ω. The trial frequency r_0 is assumed to be 10^{12} Hz, which roughly agrees with previous values[17,32]. Our general conclusions are largely insensitive to the choice of r_0. The simulation parameters are tabulated in the Supplementary Table 1.

Data availability

The data that support the findings of this study have been deposited in the GitHub database: https://github.com/QIL123/Approaching_Landauers_Limit, https://doi.org/10.5281/zenodo.21875779.

Code availability

The MATLAB scripts that analyze the raw data and reproduce the figures appearing in this paper have been deposited in the GitHub database: https://github.com/QIL123/Approaching_Landauers_Limit. https://doi.org/10.5281/zenodo.21875779.

References

1. Landauer, R. Irreversibility and heat generation in the computing process. *IBM J. Res. Dev.* **5**, 183 (1961).
2. Golod, T., Morlet-Decarnin, L. & Krasnov, V. M. Word and bit line operation of a 1 × 1 μm^2 superconducting vortex-based memory. *Nat. Commun.* **14**, 4926 (2023).
3. Krantz, P. et al. A quantum engineer's guide to superconducting qubits. *Appl. Phys. Rev.* **6**, 021318 (2019).
4. Nsanzineza, I. & Plourde, B. L. T. Trapping a single vortex and reducing quasiparticles in a superconducting resonator. *Phys. Rev. Lett.* **113**, 117002 (2014).
5. Bafia, D. et al. Quantifying trapped magnetic vortex losses in niobium resonators at mK temperatures. *Appl. Phys. Lett.* **127**, 152601 (2025).
6. Read, N. & Green, D. Paired states of fermions in two dimensions with breaking of parity and time-reversal symmetries and the fractional quantum Hall effect. *Phys. Rev. B* **61**, 10267 (2000).
7. Ivanov, D. A. Non-abelian statistics of half-quantum vortices in p-wave superconductors. *Phys. Rev. Lett.* **86**, 268 (2001).
8. Stern, A. & Lindner, N. H. Topological quantum computation—from basic concepts to first experiments. *Science* **339**, 1179 (2013).
9. Golosovsky, M. A., Snortland, H. J. & Beasley, M. R. Nonlinear microwave properties of superconducting Nb microstrip resonators. *Phys. Rev. B* **51**, 6462 (1995).
10. Embon, L. et al. Imaging of super-fast dynamics and flow instabilities of superconducting vortices. *Nat. Commun.* **8**, 85 (2017).
11. Dobrovolskiy, O. V. et al. Ultra-fast vortex motion in a direct-write Nb-C superconductor. *Nat. Commun.* **11**, 3291 (2020).
12. Clem, J. R. "AC losses in type-II superconductors". in *Magnetic Susceptibility of Superconductors and Other Spin Systems* (eds. Hein, R. A., Francavilla, T. L. & Liebenberg, D. H.) (Springer, 1991).
13. Raes, B. et al. Local mapping of dissipative vortex motion. *Phys. Rev. B* **86**, 064522 (2012).
14. Raes, B. et al. Closer look at the low-frequency dynamics of vortex matter using scanning susceptibility microscopy. *Phys. Rev. B* **90**, 134508 (2014).
15. Timmermans, M., Samuely, T., Raes, B., Van de Vondel, J. & Moshchalkov, V. V. Dynamic visualization of nanoscale vortex orbits. *ACS Nano* **8**, 2782 (2014).
16. Van de Vondel, J., Raes, B., Silhanek, A. V. Probing vortex dynamics on a single vortex level by scanning ac-susceptibility microscopy. in *From Basic Research to Applications* (eds Wördenweber, R., Moshchalkov, V., Bending, S., Tafuri, F.) (De Gruyter, 2017).
17. Embon, L. et al. Probing dynamics and pinning of single vortices in superconductors at nanometer scales. *Sci. Rep.* **5**, 7598 (2015).
18. Willa, R., Geshkenbein, V. B. & Blatter, G. Hessian characterization of the pinning landscape in a type-II superconductor. *Phys. Rev. B* **105**, 144504 (2022).
19. Bishop-Van Horn, L., Mueller, E. & Moler, K. A. Vortex dynamics induced by scanning SQUID susceptometry. *Phys. Rev. B* **107**, 224509 (2023).
20. Foltyn, M., Norowski, K., Savin, A. & Zgirski, M. Quantum thermodynamics with a single superconducting vortex. *Sci. Adv.* **10**, eado4032 (2024).
21. Kalashnikov, D. S. et al. Demonstration of a Josephson vortex-based memory cell with microwave energy-efficient readout. *Commun. Phys.* **7**, 88 (2024).
22. Vasyukov, D. et al. A scanning superconducting quantum interference device with single electron spin sensitivity. *Nat. Nanotechnol.* **8**, 639 (2013).
23. Anahory, Y. et al. SQUID-on-tip with single-electron spin sensitivity for high-field and ultra-low temperature nanomagnetic imaging. *Nanoscale* **12**, 3174 (2020).
24. Keren, I. et al. Chip-integrated vortex manipulation. *Nano Lett.* **23**, 4669 (2023).
25. Halbertal, D. et al. Nanoscale thermal imaging of dissipation in quantum systems. *Nature* **539**, 407 (2016).
26. Zeldov, E., Clem, J. R., McElfresh, M. & Darwin, M. Magnetization and transport currents in thin superconducting films. *Phys. Rev. B* **49**, 9802 (1994).
27. Gammaitoni, L., Hänggi, P., Jung, P. & Marchesoni, F. Stochastic resonance. *Rev. Mod. Phys.* **70**, 223 (1998).
28. Bérut, A. et al. Experimental verification of Landauer's principle linking information and thermodynamics. *Nature* **483**, 187 (2012).
29. Saira, O.-P. et al. Nonequilibrium thermodynamics of erasure with superconducting flux logic. *Phys. Rev. Res.* **2**, 013249 (2020).
30. Gaudenzi, R., Burzurí, E., Maegawa, S., van der Zant, H. S. J. & Luis, F. Quantum Landauer erasure with a molecular nanomagnet. *Nat. Phys.* **14**, 565 (2018).
31. Bespalov, A. A. & Mel, A. S. 'nikov, "Abrikosov vortex pinning on a cylindrical cavity inside the vortex core: formation of a bound state and depinning. *Supercond. Sci. Technol.* **26**, 085014 (2013).
32. Perego, M. et al. Experimental detection of vortices in magic-angle graphene. *Nat. Commun.* **16**, 10259 (2025).

Acknowledgements

We want to thank Oded Agam, Oren Raz, Alejandro Silhanek, Joris van den Vondel, Shlomi Kotler, Valla Fatemi, Oded Millo, and Eli Zeldov for fruitful discussions. Fabrication for this project was carried out at the Harvey Kruger Center for Nano Science and Nano Technology at the Hebrew University.

Author contributions

Y.A., H.S., I.K., and N.F. conceived the experiment. N.K. and N.F. fabricated the Nb device. N.F. conducted the scanning SOT measurements. N.F., I.K., Y.Z., H.S., R.W., and Y.A. analyzed and interpreted the data. Y.A., N.F. and R.W. conceived the numerical simulations. Y.A. and A.N. constructed the scanning SOT microscope. M.E.H. conceived the SOT readout electronics. Y.A., H.S. and N.F. wrote the article with contributions from all authors.

Funding

Y.A. acknowledges the support from the European Research Council (ERC) Consolidator Grant No. 101124770 (MAJOR). H.S. acknowledges funding by ISF grant 164/23 and BSF grant 2022122. N.K. acknowledges support from EU project OpenSuperQPlus and ISF grant 2128/24. Y.A. acknowledges support from COST Action SUPERQUMAP/CA21144.

Competing interests

The authors declare no competing interests.

Additional information

Supplementary information The online version contains supplementary material available at https://doi.org/10.1038/s41467-026-77988-x.

Correspondence and requests for materials should be addressed to Nofar Fridman, Hadar Steinberg or Yonathan Anahory.

Peer review information *Nature Communications* thanks Vladimir Fomin, and the other, anonymous, reviewer(s) for their contribution to the peer review of this work. A peer review file is available.

Reprints and permissions information is available at http://www.nature.com/reprints

Publisher's note Springer Nature remains neutral with regard to jurisdictional claims in published maps and institutional affiliations.

Open Access This article is licensed under a Creative Commons Attribution-NonCommercial-NoDerivatives 4.0 International License, which permits any non-commercial use, sharing, distribution and reproduction in any medium or format, as long as you give appropriate credit to the original author(s) and the source, provide a link to the Creative Commons licence, and indicate if you modified the licensed material. You do not have permission under this licence to share adapted material derived from this article or parts of it. The images or other third party material in this article are included in the article's Creative Commons licence, unless indicated otherwise in a credit line to the material. If material is not included in the article's Creative Commons licence and your intended use is not permitted by statutory regulation or exceeds the permitted use, you will need to obtain permission directly from the copyright holder. To view a copy of this licence, visit http://creativecommons.org/licenses/by-nc-nd/4.0/.

© The Author(s) 2026